The Astrophysical Journal, 659:1382–1393, 2007 April 20

GAS AND DUST CONDENSATIONS AND A PECULIAR CLASS 0 OBJECT IN THE LUPUS 3 STAR-FORMING CLOUD

K. Tachihara[1]
Graduate School of Science and Technology, Kobe University, 1-1 Rokko-dai, Nada-ku, Kobe, 657-8501, Japan; tatihara@kobe-u.ac.jp

M. Rengel[2]
Thüringer Landessternwarte, Tautenburg, Germany

Y. Nakajima and N. Yamaguchi
National Astronomical Observatory of Japan, Mitaka, Tokyo 181-8858, Japan

P. André
CEA Service d'Astrophysique, Saclay, France

R. Neuhäuser
Astrophysikalisches Institut und Universitäts-Sternwarte Jena, Schillergäßchen 2-3, D-07745, Jena, Germany

T. Onishi and Y. Fukui
Department of Astrophysics, Nagoya University, Chikusa-ku, Nagoya, 464-8602, Japan

and

A. Mizuno
Solar-Terrestrial Environment Laboratory, Nagoya University, Chikusa-ku, Nagoya, 464-8601, Japan
Received 2006 July 17; accepted 2006 December 20

ABSTRACT

The Lupus 3 molecular cloud has been surveyed for dense gas and dust cores and embedded objects in radio [$H^{13}CO^+$ $J = 1$–0 line and 1.2 mm continuum] and infrared [$JHK_sL'M$ N1 bands and H_2 $v = 1$–0 $S(1)$ line] wavelengths. These observations unveil a filamentary cloud, three dense cores, an embedded millimeter-wave source (MMS), and an associated elongated object in the K band. The properties of the three dense cores are $M = 3.5$–5.6 $M_\odot$, $R = 0.04-0.06$ pc, and $n(H_2) = (1.0–3.9) \times 10^5$ cm^{-3}, properties similar to those in Taurus. Two of these three objects are likely to be prestellar cores, while the other one exhibits ongoing star formation. The spectral energy distribution (SED) analysis of the MMS shows that it is a remarkably cold Class 0 object with molecular outflow detected in the CO($J = 3$–2) line and peculiar near-IR detections. From the estimated low bolometric temperature (39.5 K), faint bolometric luminosity (0.16 $L_\odot$), and sufficiently large envelope mass (0.52 $M_\odot$), the MMS is expected to be in a very early phase ($\sim 10^4$ yr) of mass accretion. The K-band elongated feature appears to be scattered light originating from the embedded central object of the MMS seen through the outflow cavity opening toward HH 78 on the near side as shown by the blueshifted CO wings. The MMS has also been detected by the *Spitzer Space Telescope*, and its near-IR images exhibit butterfly-shaped nebulosity emission as scattered light through the bipolar cavities in contrast to that in the K band. Together with the *Spitzer* and NTT *JHK* photometric data, the observed SED has a short-wavelength cutoff suggesting a low effective temperature (<1400 K) of the central object.

Subject headings: dust, extinction — ISM: clouds — ISM: individual (Lupus cloud) — ISM: jets and outflows — stars: formation — stars: pre–main-sequence

1. INTRODUCTION

The physical properties of young protostars have not been well studied because they are deeply embedded in dense molecular cloud cores, heavily obscured by the envelope material, and rare due to their short dynamical lifetimes. Recent developments in millimeter- and submillimeter-wave observational techniques have revealed such deeply embedded very young protostars as (sub)millimeter-wave point sources, and our understanding of the initial condition of star formation has significantly progressed. The protostars are categorized in terms of the spectral energy distribution (SED) of their surrounding dust material. Very young protostars, so-called Class 0 objects, are in the main accretion phase and are believed to have rich envelope material whose mass ($M_{\rm env}$) is greater than the stellar mass (M_*), which absorbs light from the central object and reradiates the emission mainly in submillimeter wavelengths (André et al. 1993). Therefore, the submillimeter-wave ($\lambda > 350$ μm) to bolometric luminosity ratio ($L_{\rm sub\text{-}mm}/L_{\rm bol}$) of Class 0 objects is larger (typically >0.5%) than that of more evolved stars, and the characteristic bolometric temperature ($T_{\rm bol}$) is less than 70 K (Myers et al. 1998; André et al. 2000). In most cases, they are associated with molecular outflows, which is another indication of young protostars. Froebrich (2005) compiled 95 confirmed and candidate Class 0 objects and summarized their physical properties. Objects in an even younger phase of star formation are called prestellar cores, which exhibit no embedded point source. They are detected in molecular emission lines of high-density tracers such as $H^{13}CO^+$ and N_2H^+, as well as in millimeter- and submillimeter-wave dust continuum emission. Surveys for dense cores and embedded protostars enable us

[1] Also at: Astrophysikalisches Institut und Universitäts-Sternwarte Jena, Jena, Germany.
[2] Current address: Max-Planck-Institute für Sonnensystemforschung, Katlenburg-Lindau, Germany.

to link Class 0 objects and prestellar cores together, and their statistics reveal their evolution timescales if they are sampled uniformly and completely from the entire cloud by a large-scale survey. However, only a handful of Class 0 objects have been found in nearby (<200 pc from the Sun) star-forming regions (SFRs), and their physical properties and evolution timescale are not yet well studied due to poor statistics.

The Lupus molecular cloud complex is one of the nearby ($d \simeq$ 150 pc) SFRs; the total molecular mass is estimated to be $1.7 \times 10^7\ M_\odot$ (Tachihara et al. 2001). It consists of several dark clouds (Cambrésy 1999) and is thought to be under the influence of Sco OB associations (Tachihara et al. 2001). Among them, Lupus 3 is the most active cloud, associated with more than 40 T Tauri stars (T associations found by Schwartz 1977) and the Herbig Ae/Be stars HR 5999 and HR 6000 distributed within $\sim$1 pc[2]. Molecular line observations of CO isotopes revealed that Lupus 3 is a filamentary cloud whose mass in ^{13}CO is 300 $M_\odot$, implying a high star formation efficiency (SFE) of $\geq$3.8% (Tachihara et al. 1996), and the C^{18}O core, defined as the half-maximum contour of the peak intensity, has relatively high mass (26 $M_\odot$) and density (8.6×10^3 cm^{-3}; Hara et al. 1999). This marginally clustering property is compared with those in other isolated SFRs such as Lupus 1 and Taurus (with a young stellar surface density of $\sim$1 pc^{-2}; Tachihara et al. 1996; Cohen & Kuhi 1979; Herbig & Bell 1988) and richer and denser clusters such as the ρ Oph and Cha I clouds ($\gtrsim$200 pc^{-2}; Comeron et al. 1993; Oasa et al. 1999). In spite of the high star formation activity, the T-association members are reported to be relatively old, at 6.7 Myr on average (Hughes et al. 1994). However, the cloud seems to have the potential to form more association members with sufficient remaining gas mass. In the Lupus region, the first Class 0 object found was Barnard 228 (Shirley et al. 2000). With relatively warm $T_{\rm bol}$ (61 K), this is believed to be a borderline object between Class 0 and I. Overall properties of the Lupus clouds and their associated young stars are well summarized in a review by F. Comeron (2007, in preparation).

In order to further investigate sites of ongoing and near future star formation in this cloud, we have carried out searches for dense cores and embedded young protostars in H^{13}CO$^+$ $J = 1$–0 and in the dust continuum at 1.2 mm. In addition, follow-up infrared observations have been performed to investigate the nature of the embedded object together with the *Spitzer* archived data at various wavelengths.

2. OBSERVATIONS

The C^{18}O cores found by Hara et al. (1999) with the NANTEN telescope have been surveyed for denser and more compact cores in the H^{13}CO$^+$ $J = 1$–0 emission line at 86.75433 GHz by the Swedish-ESO Submillimetre Telescope (SEST) at La Silla observatory in Chile. The mapping observations toward high column density regions in the C^{18}O cores were carried out in 1999 January with 30″ grid spacing with a half-power beamwidth (HPBW) of 57″ using the frequency-switching technique with a switching interval of 6 MHz. A cubic polynomial function was applied to the spectra to remove the standing wave at the continuum level. The system temperature and frequency resolution were 150 K (single-sideband) and 80 kHz, respectively, and a rms noise temperature of 0.1 K channel^{-1} was achieved with 60–120 s integration time. The spectra are divided by the main beam efficiency (0.75) to obtain $T_{\rm MB}$. In total, spectra toward 1170 positions were taken from 14 C^{18}O cores in Lupus 1–5; 236 of them were from Lupus 3. In this paper, we report the results only for the Lupus 3 cloud (core No. 27 in Hara et al. 1999). A summary of all 10 of the H^{13}CO$^+$ cores found in Lupus will be published elsewhere (A. Hayashi et al. 2007, in preparation).

The 1.2 mm continuum observation was made with the SIMBA bolometer array on SEST, whose beam size is 23″ (FWHM), on the night from 2003 May 17 to 18. In total, 21 sets of standard fast scanning mapping (scanning speed 80″ s^{-1}) centered at (R.A., decl.)$_{\rm J2000.0}$ = ($16^{\rm h}09^{\rm m}26^{\rm s}$, $-39^\circ06'06''$) with a size of 960″ × 720″ in azimuth and elevation were taken. Telescope pointing, focus, and atmospheric opacity were checked every 2 hr, and flux calibration was applied by observing Mars. The net exposure time for the total co-added field was about 4 hr. The rms noise fluctuation at the map center is 24 mJy beam^{-1}, and the typical value is $\sim$35 mJy beam^{-1}. Data reduction was achieved using the MOPSIC software package (see Chini et al. 2003).

A molecular outflow survey was carried out in the ^{12}CO $J =$ 3–2 emission line with the Atacama Submillimeter Telescope Experiment (ASTE). It has a 10 m dish whose HPBW at 345 GHz is 22″, and it is equipped with a double-sideband SIS (superconductor-insulator-superconductor) receiver and a 1024 channel autocorrelation spectrograph. These have typical performances of $T_{\rm sys} \sim$ 400 K (double-sideband) and $\Delta V = 0.11$ km s^{-1}. For five points in the *K*-band extended emission feature, position-switching observations with 8 minute integration (on-source) were performed, and a rms noise temperature of 0.18 K was achieved. The off position is chosen at (R.A., decl.)$_{\rm J2000.0}$ = ($16^{\rm h}06^{\rm m}16.4^{\rm s}$, $-39^\circ02'13.9''$), being free from the CO emission. The pointing error was checked every 2–3 hr during the observing run. The antenna temperature was calibrated by obtaining the spectra of M17 SW (R.A., decl.)$_{\rm J2000.0}$ = ($18^{\rm h}20^{\rm m}23.1^{\rm s}$, $-16^\circ11'43''$) as a standard, whose radiation temperature (T_R^*) is assumed to be 69.6 K (Wang et al. 1994).

The follow-up infrared observations toward the field centered at ($16^{\rm h}09^{\rm m}18.4^{\rm s}$, $-39^\circ04'54''$) were carried out in the $JHK_sL'M$N1 bands. The ESO 3.58 m New Technology Telescope (NTT) with the SofI detector was used for the JHK_s observations, the ESO Very Large Telescope (VLT) UT1 with ISAAC for the L' band, and the ESO 3.6 m telescope with the TIMMI2 detector for the *M*- and N1-band imaging observations. In addition to these, H_2 $v = 1$–0 $S(1)$ molecular emission at 2.12 μm was surveyed in the *K*-band extended emission by the Subaru telescope with the CISCO detector. In order to subtract the continuum emission, the N204 narrowband filter at 2.033 μm with a bandwidth of 0.020 μm was also employed. The properties of these near-IR observations are summarized in Table 1.

3. RESULTS

3.1. H^{13}CO$^+$ *Cores*

Figure 1 (*left*) shows the H^{13}CO$^+$ integrated intensity map overlaid with the C^{18}O map of Hara et al. (1999). Three spherical condensations are illustrated in the elongated ridge of the C^{18}O core. They are located offset to the east from the C^{18}O peak inside the core, whereas no H^{13}CO$^+$ emission was detected near the C^{18}O peak. These disagreements of the peak positions in different tracers are discussed in § 4.1.

No T Tauri stars are associated with the H^{13}CO$^+$ condensations, and thus no dense molecular gas remains toward the T association. Hence, no more star formation is expected in the western edge of the filament but instead there are potential sites of star formation in the eastern part of the cloud, where H^{13}CO$^+$ is detected. These three H^{13}CO$^+$ condensations have slightly elongated spherical shapes and are expected to be in a gravitationally bound state (Onishi et al. 2002). We define the three H^{13}CO$^+$ cores using contours of the half-maximum level of the local peaks and then

TABLE 1
PROPERTIES OF THE NEAR-IR OBSERVATIONS

Band	Wavelength (μm)	Telescope and Instrument	Field of View (arcsec)	Pixel Scale (arcsec pixel^{-1})	Exposure (minutes)	5 σ Limiting Magnitude (mag)	Date (UT)
J	1.247	NTT SofI	144 × 144	0.144	54	22.5	2004 Apr–May
H	1.653	NTT SofI	144 × 144	0.144	35	18.9	2004 Apr–May
K_s	2.162	NTT SofI	144 × 144	0.144	92	19.7	2004 Apr–May
L'	3.78	VLT-UT1 ISAAC	73 × 73	0.071	16	12.1	2005 May 8
M	4.64	ESO 3.6 m TIMMI2	96 × 76	0.3	32	6.18	2004 May 12
N1	8.70	ESO 3.6 m TIMMI2	64 × 48	0.2	50	5.02	2004 May 12
H_2	2.12	Subaru CISCO	108 × 108	0.105	38	6.9[a]	2004 Jul 10
N204	2.033	Subaru CISCO	108 × 108	0.105	33	...	2004 Jul 10

[a] 3 σ limiting flux of the surface brightness in units of 10^{-2} mJy arcsec^{-2}.

derive the physical parameters of the cores as follows. They roughly coincide in positions and shapes with the previously identified infrared dark cores named A, B, and C by Nakajima et al. (2003) or cores C, D, and E by Teixeira et al. (2005), whose A_V are larger than 20 mag. In accordance with Nakajima et al. (2003), we hereafter call them cores A, B, and C.

The physical parameters of the three $H^{13}CO^+$ cores are derived as follows. First, we count the number of observed points whose integrated intensities of $H^{13}CO^+$ are greater than half the peak values and multiply it by the area of the observing cell (30 arcsec^2 = 0.0005 pc^2 at a distance of 150 pc). Then the effective radii (R) of the spheres that have the same projected area are calculated. All the spectra of the above observed points were summed up to obtain composite spectra for each core. They all resemble, and are thus fitted to, single-peaked Gaussian spectra, which give the peak T_{MB}, central V_{LSR}, and ΔV. Because the absolute molecular abundance of $H^{13}CO^+$ is unknown, we employ the virial theorem to derive the core mass. Making use of these physical parameters, the virial mass (M_{vir}) is given as

$$M_{vir} = 210 R \Delta V^2 \quad (1)$$

by assuming a spherical shape, uniform density, and negligible external pressure, magnetic fields and rotation. The core shapes are assumed to be spherical for this analysis, but they are not much larger than the HPBW and might actually be elliptical or irregularly shaped. These assumptions are not necessarily guaranteed, but previous studies show that the compact dense cores are in near gravitational equilibrium, and the virial equation provides a fair estimate of the core mass (Tachihara et al. 2002;

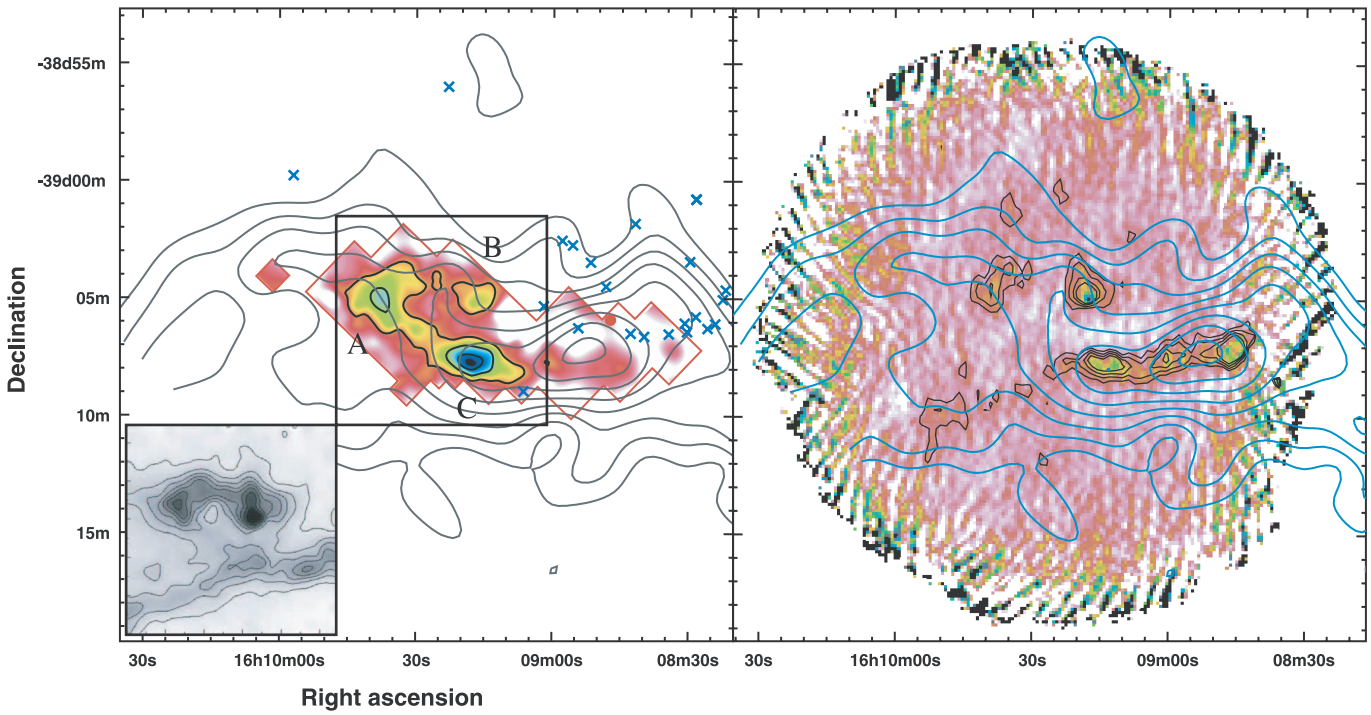

FIG. 1.—SEST observations of the Lupus 3 cloud. *Left:* $H^{13}CO^+$ integrated intensity map shown as a pseudo–color image and thick black contours (0.27 K km s^{-1} each), overlaid on the $C^{18}O$ contours (integrated intensity of 0.3 K km s^{-1} each; *thin gray contours*) taken with the NANTEN telescope by Hara et al. (1999). Gaussian smoothing with a size of 30″ is applied. The border of the surveyed area is illustrated by the red lines. The blue crosses and red filled circle are T Tauri stars (Hughes et al. 1994) and IRAS 16054−3857, respectively. The three cores are named A, B, and C as shown. The central black square denotes the area covered by the A_V map of Nakajima et al. (2003), shown in the inset. *Right:* The 1.2 mm continuum SIMBA map shown as a pseudo–color image. The black contours are from 35 to 140 mJy beam^{-1} with 35 mJy beam^{-1} steps excluding the border of the field of view. Overlaid in blue are the same $C^{18}O$ contours as in the left panel.

TABLE 2
PHYSICAL PROPERTIES OF THE $H^{13}CO^+$ CORES

Core Name	R.A.[a] (J2000.0)	Decl.[a] (J2000.0)	Galactic Longitude[a]	Galactic Latitude[a]	T_{MB}[b] (K)	V_{LSR}[b] (km s^{-1})	ΔV[b] (km s^{-1})	R (pc)	M_{vir} ($M_\odot$)	$n(H_2)$ (10^5 cm^{-3})	M_{dust}[c] ($M_\odot$)	M_{dust}[d] ($M_\odot$)	M_{dust}[e] ($M_\odot$)
A	16 09 38.4	−39 04 56	339.692	9.250	1.01	4.9	0.63	0.055	4.6	1.0	4.5	1.3	6.3
B	16 09 18.3	−39 05 10	339.642	9.292	0.72	4.8	0.66	0.039	3.5	2.1	4.1	1.2	5.7
C	16 09 19.7	−39 08 25	339.617	9.258	1.01	4.6	0.85	0.037	5.6	3.9	3.6	1.4	4.8

NOTE.—Units of right ascension are hours, minutes, and seconds, and units of declination are degrees, arcminutes, and arcseconds.
[a] Peak positions of the $H^{13}CO^+$ integrated intensity.
[b] Derived from Gaussian fitting to the composite spectra.
[c] The subtracted sky level of 13 mag is assumed.
[d] No subtracted sky level is assumed.
[e] The subtracted sky level of 20 mag is assumed.

Onishi et al. 2002). The mean molecular density of the core is given as

$$n(H_2) = \frac{3M_{vir}}{4\pi R^3 \mu m_H}, \quad (2)$$

where μ and m_H are the mean molecular weight (2.8) of the interstellar gas (taken with respect to the total number of hydrogen molecules) and the atomic hydrogen mass, respectively. These physical parameters are summarized in Table 2.

These three cores share almost similar R ($\sim$0.04 pc) and M_{vir} (3.5–5.6 $M_\odot$) and are similar in size and slightly more massive due to larger ΔV than the $H^{13}CO^+$ cores in Taurus (Onishi et al. 2002). Relatively large ΔV implies that the cores in Lupus have a larger amount of turbulence than in Taurus. The difference in ΔV among the regions was also seen in the sample of $C^{18}O$ cores and discussed in conjunction with their dynamical stabilities by Tachihara et al. (2002). The Taurus cores have similar R on average to Lupus, although they were observed with 3 times higher spatial resolution than the present study, but some of them were undersampled. Core C has the largest ΔV and the smallest R, and therefore the largest $n(H_2)$ among all 10 samples in Lupus. It also has the largest peak integrated intensity of $H^{13}CO^+$.

If we define the core size in terms of constant intensity, the present cores have larger size dispersion, and core B with relatively weak peak intensity has the smallest extent. For the case of 0.5 K km s^{-1} as the core boundary, the three cores have radii of 0.051, 0.021, and 0.046 pc, respectively. These can arbitrarily change with the definition. On the other hand, the core radius defined by the half-maximum intensity is more sensitive to the density gradient than the peak intensity if its density (and thus column density) profile follows a power-law function. Therefore, an almost constant radius implies that the cores have similar density gradients, and the central density is primarily represented by the peak intensity.

3.2. 1.2 mm *Dust Continuum*

Figure 1 (*right*) shows the 1.2 mm continuum observation by SIMBA. In this region, significant detections of dust condensations that correspond to the three $H^{13}CO^+$ cores are noticeable. In core B, a centrally peaked point source is seen as being an embedded object. In addition to these dust condensations, a filamentary feature along the $C^{18}O$ ridge is detected. The dust filament stretches to the $C^{18}O$ peak, where the 1.2 mm emission has local peaks near the center of the $C^{18}O$ peak, in contrast to the nondetection of the $H^{13}CO^+$ emission there. Part of the image near the outer boundary has poor signal-to-noise ratio because of minimal overlapping of each scan. However, the mismatch between the $H^{13}CO^+$ and the continuum emission is particularly obvious around the $C^{18}O$ peak. This is because the dust continuum is a column density tracer, similar to the $C^{18}O$ emission.

3.2.1. *Extended Emission*

In order to further investigate distributions of the continuum and $H^{13}CO^+$ emission, we make detailed comparisons with the extinction map taken in near-IR by Nakajima et al. (2003), K. Dobashi (2006, private communication, from Two Micron All Sky Survey [2MASS] data), and Teixeira et al. (2005). All of these extinction data are derived from the color excess in the *JHK* bands. General distribution of the 1.2 mm continuum resembles the dust extinction, and the three cores and the filamentary structure are well traced by Nakajima et al. (2003; see Fig. 1, *inset*) and Teixeira et al. (2005), while the cores are not resolved by the 2MASS data because of the heavy extinction and small number of available background stars in the shallow survey. The $H^{13}CO^+$ observation does not show the filamentary structure but only the three dense cores.

The extinction is not as strong as the other two in core C (alternatively named core E in Teixeira's nomenclature), whose peak A_V is less than 25 mag, where the 1.2 mm continuum and the $H^{13}CO^+$ emissions are relatively strong. The peak position of the 1.2 mm continuum is placed in a hollow in the extinction map between the Teixeira's cores E and F. By comparing with the three-color image given by Nakajima et al. (2003), we discovered it to be a region of heavy extinction ($A_V \geq 20$ mag) with practically no available background star, which resulted in an underestimation of the A_V and a fake hollow in the filament. Core B has a smaller extent in $H^{13}CO^+$ than in the 1.2 mm continuum and dust extinction, while the part of the $H^{13}CO^+$ emission connecting cores A and C is missing in the continuum map. There might be chemical effects that make a local abundance anomaly of $H^{13}CO^+$ molecules in the cores or a local temperature rise that enhances the dust emissivity.

For the three cores, we estimated the mass derived from the dust continuum (M_{dust}). In millimeter wavelengths, the dust emission is optically thin, and hence the millimeter-wave flux is in principle proportional to the molecular column density [$N(H_2)$], if the dust temperature (T_{dust}), grain properties, and dust-to-gas ratio are constant. It is given as

$$N(H_2) = \frac{S}{\Omega_{MB}\mu m_H \kappa B(T_{dust})}, \quad (3)$$

where S is the flux density at 1.2 mm, Ω_{MB} is the main beam solid angle, κ is the dust opacity per unit mass column density at 1.2 mm, and $B(T)$ is the Planck function for the temperature T. In

the Rayleigh-Jeans approximation and with assumptions of $T_{\rm dust} = 20$ K and $\kappa = 0.005$ cm^2 g^{-1}, the above equation is described as (Motte et al. 1998)

$$N(\mathrm{H_2}) \approx \left(\frac{S}{10\ \mathrm{mJy/23''\ beam}}\right)\left(\frac{T_{\rm dust}}{20\ \mathrm{K}}\right)^{-1} \times \left(\frac{\kappa}{0.005\ \mathrm{cm^2\ g^{-1}}}\right)^{-1} \times 10^{21}\ \mathrm{cm^{-2}}. \quad (4)$$

In order to derive the mass, $N(\mathrm{H_2})$ within the core has to be summed up. However, in the process of data reduction, a diffuse component of the flux that extends over each scan field is subtracted as a constant sky level with the MOPSIC baseline determination process. In order to make the mass estimate consistent with other wavelengths, we compare the continuum map with the extinction maps of Nakajima et al. (2003), K. Dobashi (2006, private communication), and Teixeira et al. (2005), as mentioned above, and found that the detection limit intensity level of 35 mJy beam^{-1} roughly corresponds to $A_V \simeq 20$ mag. Teixeira et al. (2005) subtracted 9 and 6 mag from cores A and B, respectively, as diffuse background plateaus surrounding the cores to derive the mass. Taking into account the typical plateau level of 7 mag, we add 13 mag (2.5×10^{22} cm^{-2}) to $N(\mathrm{H_2})$ for consistency. This results in $\sim$3 $M_\odot$ of extra mass for each core. For comparison, the masses are also calculated with the assumed plateau levels of 0 and 20 mag. For core B, the point source is subtracted as a Gaussian PSF. Then $N(\mathrm{H_2})$ of each data pixel is summed up and multiplied by μ and $m_{\rm H}$. The obtained dust masses $M_{\rm dust}$ are 4.5, 4.1, and 3.6 $M_\odot$ for cores A, B, and C, respectively (Table 2). These are consistent with those derived from extinction by Teixeira et al. (2005).

3.2.2. *Millimeter-Wave Point Source*

In addition to these extended features, a point source was detected in the 1.2 mm continuum. It is clearly embedded in core B and thus seems to be a young protostar. It has no counterpart among previously known young stellar objects and is located 1.16′ ($\sim$10,000 AU at the distance of 150 pc) away from HH 78. The millimeter-wave point source (MMS) is illustrated with a Gaussian profile slightly larger than the point-spread function (PSF) of the SEST beam (24″ HPBW; Fig. 2). Gaussian fitting to the point source gives the center coordinates and the FWHM size of (R.A., decl.)$_{\rm J2000.0}$ = ($16^{\rm h}09^{\rm m}18.33^{\rm s}$, $-39^\circ04'51.6''$) and $\sim$26″, respectively, as a convolution of the point source and the SEST beam.

The radial profile of the MMS is investigated by averaging the 1.2 mm flux within each annulus with a width of 10″ centered at the peak position as a function of the radial distance. The convolution of the fitted profile with the 24″ Gaussian beam gives a source size of $\sim$10″, $\sim$750 AU radius at a distance of 150 pc. PSF photometry gives a 1.2 mm flux of 0.63 $\pm$ 0.04 Jy. The MMS has a surrounding envelope that is smoothly connected with the extended component up to $\sim$50″, which is almost the size of the $\mathrm{H^{13}CO^+}$ core ($\sim$7800 AU). Outside this radius, the profile declines steeply, showing a clear boundary. The radial profile of the envelope is fitted to a power-law function between radii of 20″ and 50″, and it yields a power-law index of -0.8 ± 1.5. This is slightly shallower than but consistent with other embedded protostars and steeper than prestellar cores (Shirley et al. 2000; Motte & André 2001; Rengel 2004). Our sample has, however, large uncertainty of the power-law index partly because of the fan-shaped structure (see § 3.3) and poor spatial resolution. The structure of the MMS should be investigated in more detail with higher resolution observations.

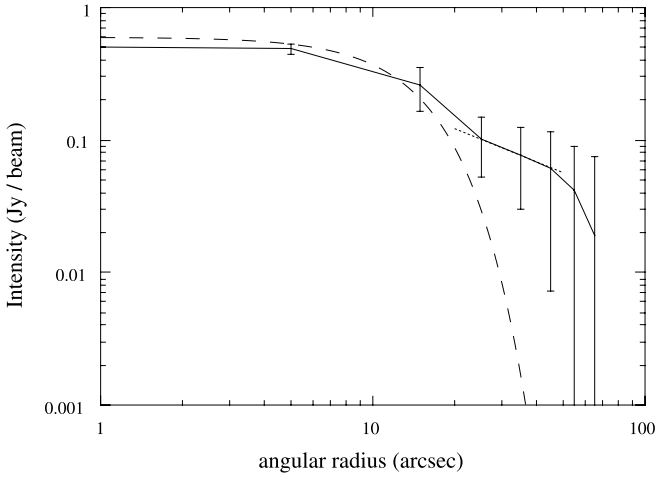

FIG. 2.—Radial profile of the 1.2 mm emission around the MMS. The flux is averaged over each annulus with a width of 10″. The error bars show the standard deviation of the flux within each annulus. The dashed line represents the Gaussian beam with a FWHM of 24″. The dotted line is a power-law function fitted to the data points between 20″ and 50″ in radius with a power-law index of -0.8.

In order to estimate the envelope mass, $M_{\rm env}^{4200\ \rm AU}$, aperture photometry for the MMS is employed with a chosen aperture size of 28″ (4200 AU) in radius for a direct comparison with other objects by Motte & André (2001). With a sufficiently large annulus to avoid confusion with the extended core component, the aperture integrated flux is estimated to be $F_{1.2\ \rm mm}^{\rm int} = 0.99 \pm 0.13$ Jy. The envelope mass is then measured as proportional to the optically thin 1.2 mm emission following Motte & André (2001). Their previous studies suggested a mass-averaged dust temperature of 15 K for a low-luminosity object such as those in Taurus. By taking a slightly lower $T_{\rm dust} = 15$ K and a slightly larger $\kappa = 0.01$ cm^2 g^{-1} than in § 3.2.1, the envelope mass of the MMS is estimated to be $M_{\rm env}^{4200\ \rm AU} = 0.52\ M_\odot$. As shown by equation (4), the envelope mass is inversely proportional to $T_{\rm dust}$ and κ. Therefore, the arbitrariness of these values is directly attributed to the uncertainty of the derived mass. In particular, the behavior of κ is not well known, and thus it may have an uncertainty of a factor of a few. The appropriateness of this dust temperature is further examined in § 4.3.1. The derived envelope mass is comparable to the largest protostellar envelope mass measured by Motte & André (2001) in Taurus and very similar to that of the Class 0 object of IRAM 04191+1522. The nature of the MMS is further discussed in § 4.

3.3. *Infrared Data*

The NTT images in JHK_s are shown in Figure 3. The position of the MMS is marked as a plus sign. In the J and H bands, nothing is detected around the MMS except for the diffuse and faint emission west of the MMS. This is mentioned as a "fan-shaped structure" by Nakajima et al. (2003) that is part of the low extinction. On the other hand, the K-band image clearly shows an extended emission feature that has a cometary shape pointing toward the MMS. This K-band extended feature was also found by Nakajima et al. (2003) and confirmed by the present image with more detailed structure at higher resolution. Nakajima et al. (2003) suggested that this emission is a jet coming from a hidden young protostar and physically associated with IRAS 16059−3857 and HH 78. The aperture photometry for this extended

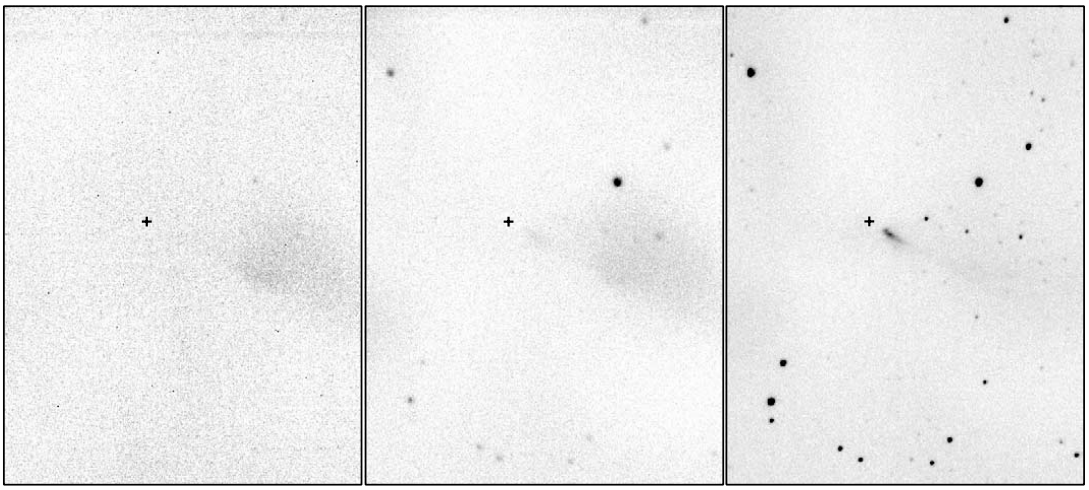

FIG. 3.—*J*, *H*, and *K* images near the Lupus 3 MMS (*from left to right*). The center and the size of the images are ($16^{h}09^{m}17.71^{s}$, $-39^{\circ}04'56.2''$) and $1.2' \times 1.6'$, respectively. The plus signs show the positions of the MMS.

K-band feature gives $K_s = 16.1 \pm 0.2$ mag, consistent with Nakajima et al. (2003).

In the longer wavelength of the $L'M$ N1 bands, no apparent detection was obtained with the present limiting magnitudes.

In order to investigate where the *K*-band emission comes from, the shock-excited H_2 $v = 1$–0 $S(1)$ line was observed. The Subaru image shown in Figure 4 (*left*) shows a clear detection similar to the *K*-band extended feature that is associated with the MMS. The N204 narrowband image is removed from the H_2 image in order to subtract the continuum component, and the residual image is shown in Figure 4 (*right*). The extended emission feature is not clearly visible in the residual image, while HH 78 remains as a slightly elongated emission feature indicating that it is excited by a shock. This implies that the *K*-band extended feature is not shock-excited emission but scattered light coming from the embedded central object.

We suggest that the central object of the MMS has an invisible jet or outflow that swept out the material and created the conical cavity of the core, with the light scattered on its surface. The cavity appears to be a notch of the core with relatively low extinction referred to as the fan-shaped structure by Nakajima et al. (2003; see also Fig. 6 of Teixeira et al. 2005). This hypothesis is supported by the fact that the 1.2 mm continuum emission is slightly enhanced at the low-extinction fan-shaped part (Fig. 5, *left*), probably due to heating of the dust at the cavity surface by radiation from the central young stellar object. Nakajima et al. (2003) pointed out that another fan-shaped structure visible on the northeast of the MMS might be the counterstructure, where 1.2 mm emission is depressed. Since the dust emission intensity is a proportional function of both the dust column density and temperature, the low column density may compensate for the dust heating on this side. Further high-resolution quantitative A_V measurements and multiwavelength observations in the cavities would help us investigate the dust temperature distribution.

3.4. CO($J = 3$–2) *Data*

In the above subsection, we proposed that scattered light from the embedded central object emerges through the conical cavity created by a molecular outflow and a jet, which is invisible in the shock-excited emission of the H_2 line probably because it is too faint. Molecular outflow is one of the signatures of young protostars, and it is commonly seen to be associated with Class 0/I objects. The CO $J = 3$–2 spectra were taken at five positions where the *K*-band extended feature is visible as shown in Figure 5. All five spectra exhibit blueshifted wings that extend $\sim$4 km s^{-1} from the systemic velocity. They are the evidence of molecular outflow driven by the young protostar, although its bipolarity is yet unknown due to the limited observing area. These indicate a

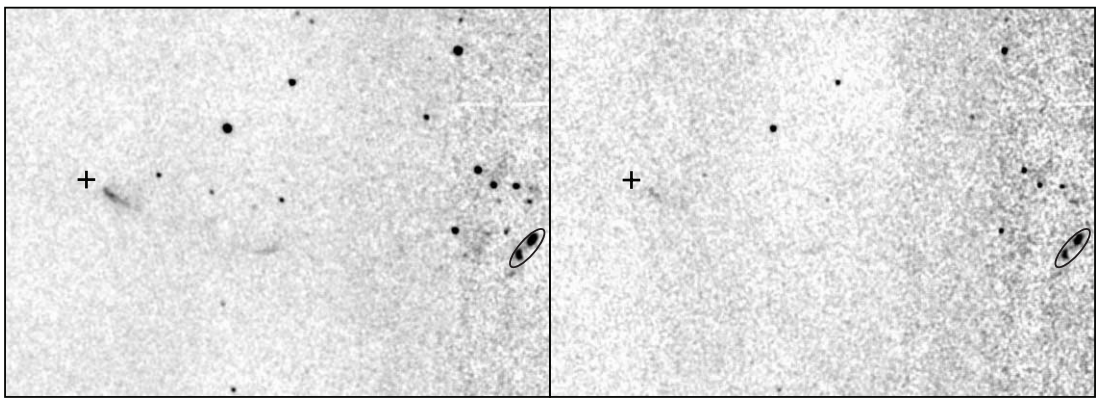

FIG. 4.—Subaru image in the H_2 narrowband filter (*left*) and residual image after the N204-band image is subtracted (*right*). The image center and the size are ($16^{h}09^{m}15.8^{s}$, $-39^{\circ}04'55''$) and $1.4' \times 1.0'$, respectively. The plus sign and ellipse mark the positions of the Lupus 3 MMS and HH 78, respectively. Boxcar smoothing with a width of 3 pixels was applied.

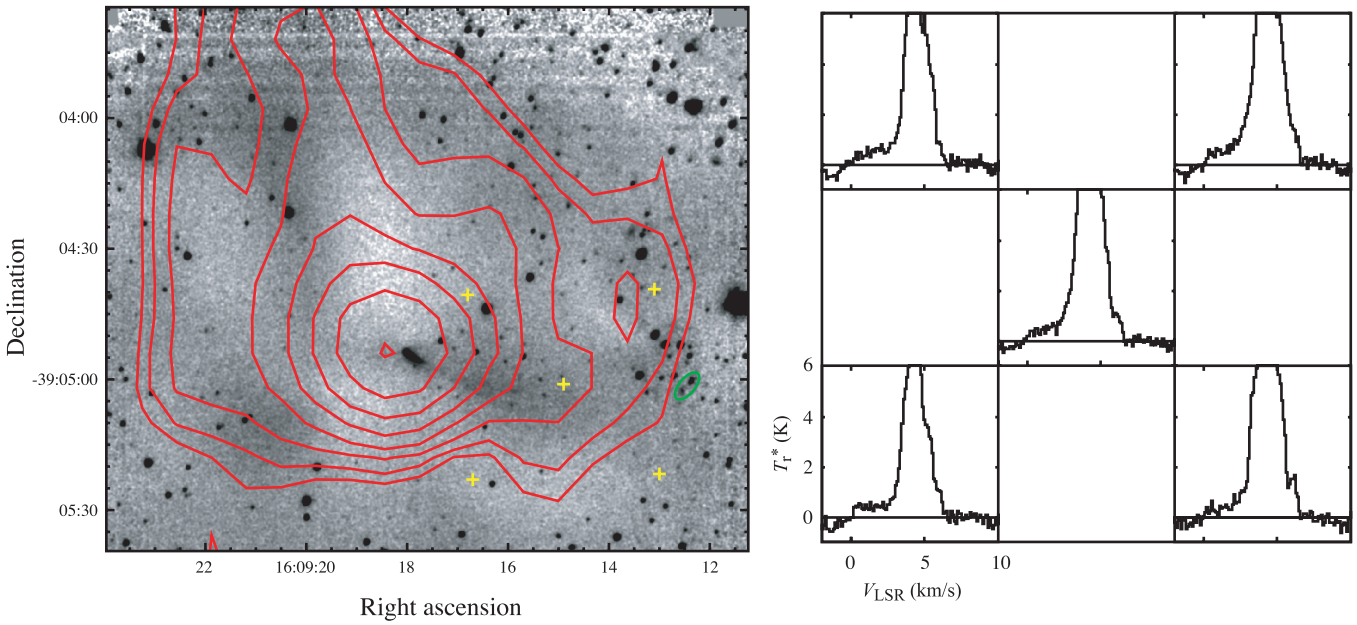

FIG. 5.—*Left:* Close-up view of the NTT K_s-band image around the MMS and core B. The intensity contrast is enhanced compared with Fig. 3. Overlaid are contours of the 1.2 mm continuum (smoothed by a 2 pixel Gaussian) from 0.035 to 0.45 Jy beam^{-1} with a logarithmic interval. The ellipse indicates HH 78. The five plus signs are the positions where the ^{12}CO($J = 3$–2) lines are observed. *Right:* Five-point spectra of the ^{12}CO($J = 3$–2) line. The blue-shifted wings around $V_{LSR} \sim 1$ km s^{-1} are clearly visible (see text).

geometric picture in which the outflow from the MMS is approaching us and is physically connected with the Herbig-Haro object HH 78, and the cavity where the *K*-band scattered light is visible is opening in the same direction. Although the extent of the molecular outflow is not determined, the dynamical age of the outflow is roughly estimated to be of the order of 5×10^3 yr by assuming the maximum extent of the lobe is ~6000 AU with a viewing angle of 45° and an outflow velocity of 5.5 km s^{-1}.

3.5. *Spitzer Data*

The *Spitzer Space Telescope* archive data on the Lupus 3 cloud recently became available, and they have been investigated in order to search for the counterpart of the MMS. The legacy program (program IDs 173 and 175 by Evans et al. 2003) and the GTO program (program ID 6 by Giovanni Fazio) covers the entire cloud in near-IR (by IRAC) and mid-IR (by MIPS). The mosaic fields of all the wavelength bands show significant detections of the MMS counterparts, contrary to the nondetection in 100 μm by *IRAS*. In the IRAC bands (3.6, 4.5, 5.8, and 8.0 μm) it appears to be a slightly elongated emission, while it seems more to be a point source in the MIPS bands (24, 70, and 160 μm bands). We employ aperture photometry in all seven bands, and the results are listed in Table 3. For the IRAC bands, elliptical apertures were used, and the sky levels were taken in a few nearby empty regions. For the MIPS data, circular apertures and appropriate aperture corrections are applied according to the *Spitzer* data handbook. Because the area coverage at 160 μm is patchy and the image is subject to latent and poor resolution in this band, the photometry has large errors. In relatively longer wavelength bands, the sky level is not uniform due to interstellar diffuse dust irradiated by nearby bright stars (HR 5999 and HR 6000). Therefore, the photometric error mainly comes from the background uncertainty, which is ~10%–40%.

In order to elucidate the geometric structure of the MMS, the positional coincidence of these emission structures in different wavelengths is investigated. Although they all have elongated shapes in the near-IR bands, the peak positions and the structures are significantly different. In the K_s band, the emission appears to be cometary in shape with a bright head and a long-stretched diffuse tail, while it is more symmetric and bipolar in structure at 3.6 and 4.5 μm, and the emitting areas are smaller at longer wavelengths. These features are illustrated in a three-color image comprising the 8.0 μm (*red*), 4.5 μm (*green*), and K_s band (*blue*) shown in Figure 6. The head of the cometary shape in the K_s band is located at the MMS position, and the tail is visible only on the western side of it (see also Fig. 5). On the other hand, the 4.5 μm emission has a butterfly-like shape that stretches both to the western and eastern sides of the MMS. This butterfly-shape emission is also visible in 3.6 μm, while in 5.8 μm it looks more like a small elliptical shape. The extent of the 8.0 μm emission is significantly smaller than those in other wavelengths at the MMS position,

TABLE 3
PHOTOMETRIC DATA OF THE LUPUS 3 MMS

Wavelength (μm)	Flux Density (Jy)	Error (Jy)	Aperture Radius[a] (arcsec)
2.2	0.22×10^{-3}	0.04×10^{-3}	7.3
3.6	1.0×10^{-3}	0.2×10^{-3}	8.4
4.5	2.9×10^{-3}	0.2×10^{-3}	8.6
5.8	1.9×10^{-3}	0.6×10^{-3}	7.6
8.0	1.0×10^{-3}	0.4×10^{-3}	6.1
24	0.031	0.003	6[b]
60	1.7	0.2	...
70	2.6	0.2	16[c]
100	<25.5[a]	...	...
160	9.3	3.7	50[d]
1200	0.99	0.13	28

[a] From the data on IRAS 16059−3857.
[b] An aperture-correction factor of 1.699 is applied.
[c] An aperture-correction factor of 1.884 is applied.
[d] An aperture-correction factor of 1.476 is applied.

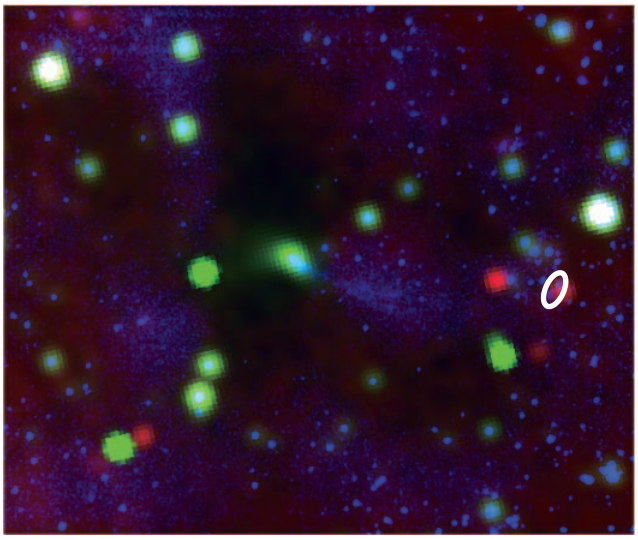

FIG. 6.—Composite three-color image (*red*, *Spitzer* 8.0 μm; *green*, 4.5 μm; *blue*, NTT K_s band) around the MMS centered at ($16^h09^m17.5^s$, $-39°04'53''$) with a size of $2.5' \times 2.2'$. The image is smoothed with a 2 pixel Gaussian. The ellipse shows the position of HH 78.

while the enclosing envelope is visible as a dark shadow, contrasted with the diffuse surrounding emission. This dark feature appears to be an ellipse whose major axis is $\sim 1.5'$ ($\sim$14,000 AU at 150 pc), almost perpendicular to the *K*-band tail and the direction to HH 78. These structural features are consistent with the geometric picture suggested above; i.e., the MMS has conical cavities in the core where the *K*-band emission is visible as scattered light only on the near side. The scattered light from the far-side countercavity is dimmed by the envelope and not visible in the K_s band, but it is detected at longer wavelengths thanks to its relatively low opacity and the high sensitivity of the *Spitzer*. The diffuse surrounding emission at 8.0 μm is probably scattered light from field stars similar to that in lower density regions in the *JHK* bands as discussed by Nakajima et al. (2003).

4. DISCUSSION

4.1. *The Volume and Column Density Distributions of Lupus 3*

The cloud structures traced by different emissions and absorptions show notable differences in the volume and column density distributions. Overall cloud structure of Lupus 3 is filamentary as illustrated by the $C^{18}O$ ridge. Its column density is basically well traced by dust emission and extinction, even though it has possible enhancement of the emissivity due to the radiation heating by nearby stars and the underestimation of the extinction due to the paucity of the background stars as mentioned in § 3.2.1. On the other hand, molecular emissions require more careful treatment of excitation condition and chemical abundance being used as tracers. The total intensity of molecular emissions with a low critical density of excitation (n_{crit}), such as CO isotopes, is in principle proportional to the molecular column density as long as it is optically thin, and thus traces the H_2 column density if the molecular abundance is constant. On the contrary, high critical density molecules such as $H^{13}CO^+$ emit only if the volume density is greater than n_{cirt} ($\sim 10^5$ cm^{-3} for the case of $H^{13}CO^+$); therefore, it is a high-density region tracer.

Near the intensity peak of $C^{18}O$, no $H^{13}CO^+$ emission is detected where 1.2 mm continuum has a local peak (see Fig. 1). It is possible that the abundance ratios of $C^{18}O$ and $H^{13}CO^+$ molecules to H_2 change depending on the cloud circumstances. Both of these molecules are reported to be depleted in some dense and cold starless cores (e.g., Lee et al. 2003). However, it is unlikely that the $H^{13}CO^+$ molecule is selectively depleted in the region where gas and dust temperature is relatively high, being irradiated by the nearby Herbig Ae/Be stars. This implies that the cloud has a relatively long path length along the line of sight at the $C^{18}O$ peak, and the volume density is less than 10^5 cm^{-3}. Moreover, detection of multivelocity components in the $C^{18}O$ lines at the $C^{18}O$ peak (Hara et al. 1999) supports the idea that molecular clouds are overlapping there. The column densities derived from the 1.2 mm continuum emission toward the $C^{18}O$ peak and core C are both $\sim 2.5 \times 10^{22}$ cm^{-2}. By assuming a uniform volume density of $\sim 10^5$ cm^{-3}, the path length of the cloud toward the continuum peak is estimated to be $\sim$0.08 pc, which roughly corresponds to the diameter of the $H^{13}CO^+$ cores. The peak column density in the NANTEN beam derived from the $C^{18}O$ peak intensity is 1.2×10^{22} cm^{-2}, and with the assumption of 10^4 cm^{-3} density, the path length is estimated to be $\sim$0.4 pc, similar to the width of the $C^{18}O$ filament. It is alternatively plausible that two 5×10^3 cm^{-3} density filaments with 0.4 pc widths are overlapping on the same line of sight at the $C^{18}O$ peak position. Therefore, a longer path length by a factor of a few with a lower volume density can easily yield local intensity peaks in $C^{18}O$ and the dust continuum. In order to search for real density peaks embedded in a diffuse molecular cloud, it is useful to combine data of a high critical density molecule with other column density tracers.

4.2. *The Dense Cores and Star Formation in Lupus 3*

We have identified three $H^{13}CO^+$ cores in Lupus 3, one star-forming core and two prestellar cores. They are compared with those in other SFRs. The Taurus molecular cloud has been surveyed for $H^{13}CO^+$ cores most comprehensively by Onishi et al. (2002). They are almost uniformly and completely surveyed from the preceding $C^{18}O$ core sample with 3 times higher spatial resolution than the present study. The mean physical parameters of radius, virial mass, average density, and line width are given as 0.048 pc, 4.0 $M_\odot$, 2.0×10^5 cm^{-3}, and 0.62 km s^{-1}, respectively, which are consistent with our results despite the different spatial resolutions. Star-forming core B in Lupus 3 shows no peculiarity in these parameters when compared with the other two non–star-forming cores. Among the 55 $H^{13}CO^+$ cores in Taurus, Onishi et al. (1999) found a peculiar core named MC 27 (also known as L1521F), which is suggested to be in the earliest phase of the star formation. It has the largest central density ($\sim 10^6$ cm^{-3}) derived from $J = 4$–3 and 3–2 transition lines of $H^{13}CO^+$ and exhibits infalling gas motion illustrated by double-peaked HCO^+ lines without any *IRAS* point source, while its average density derived only from the $H^{13}CO^+$ $J = 1$–0 data is only 1.6×10^5 cm^{-3}. In spite of the dust continuum detections in millimeter (Crapsi et al. 2004) and submillimeter wavelengths (Kirk et al. 2005), MC 27 was believed to be a prestellar core. However, it turned out to have an embedded object seen also by *Spitzer* as scattered nebulosity in near-IR (Terebey et al. 2005; Bourke et al. 2006). For this reason, MC 27 should be regarded as a very early phase Class 0 object, similar to IRAM 04191+1522. In addition, there are three more Class 0 candidates (Froebrich 2005) embedded in the Taurus cores (MC 13b, 35, and 40), which should be categorized as borderline objects with relatively warm T_{bol}. Average densities of these Class 0–harboring cores are not prominently large. This is probably because of the density gradient as discussed in detail by Onishi et al. (1999). The volume averaging of

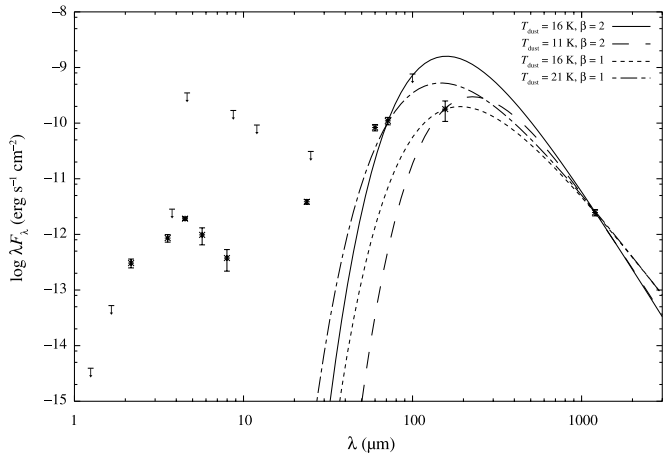

FIG. 7.—Total SED of the Lupus 3 MMS. The data points are at the K_s band (NTT), 3.6, 4.5, 5.8, 8.0, 24, 70, and 160 μm (*Spitzer*), 60 μm (*IRAS*), and 1.2 mm (SIMBA), marked by stars with error bars. The arrows at the *JHL′M* N1 bands and 12, 25, and 100 μm show the upper limits of the measurements. The curves illustrate graybody spectra with given parameter sets assuming $\tau_{100} = 1$.

the density smooths out the density gradient, which is significantly steep for MC 27. Note also that a certain fraction of matter in the star-forming cores has already been dissipated by the molecular outflow, even if the protostar is very young. In order to investigate them more in detail, we need higher resolution observations to resolve the inner structure of the dense cores.

4.3. *Spectral Energy Distribution of the Millimeter-wave Source*

Here we compile the photometric data of the MMS from the K_s-band near-IR data to the 1.2 mm radio data together with mid- to far-IR data from the *IRAS* and *Spitzer* archive. We take the integrated flux with a 4200 AU aperture radius for the 1.2 mm data, taking into account the emission from the MMS envelope. From these data, we draw the SED of the MMS as shown in Figure 7. It has two peaks and does not resemble a single-peaked blackbody spectrum but rather illustrates two-temperature spectra smoothly connected at 24 μm.

4.3.1. *Estimates of $T_{\rm bol}$ and $L_{\rm bol}$*

In order to quantitatively assess the properties of the MMS, we estimate the bolometric temperature, $T_{\rm bol}$, and luminosity, $L_{\rm bol}$, which are good indicators of stellar mass and age (Myers & Ladd 1993; Myers et al. 1998). As discussed above, fluxes in the near-IR are believed to be scattered light from the central object, while the far-IR and radio light is thermal emission. In addition, the scattered light in different wavelengths comes through different paths with different extinctions. These make the SED analysis complicated. We divide the SED into short ($\lambda \leq 8.0$ μm) and long ($\lambda \geq 60$ μm) wavelength components and investigate them separately. In this section, only the long-wavelength component is discussed; in § 4.3.2 we deal with the short one.

The long-wavelength component is thought to be thermal emission from the dust envelope where the central object is embedded. In the longer wavelength region, the radiation becomes optically thin and the SED should be treated as a graybody. Employing the optical depth of dust τ_ν, the graybody spectrum is expressed as

$$F_\nu = \Omega B(\nu, T_{\rm dust})(1 - e^{-\tau_\nu}), \tag{5}$$

TABLE 4
PHYSICAL PROPERTIES OF THE LUPUS 3 MMS

Object Name	R.A. (J2000.0)	Decl. (J2000.0)	$T_{\rm bol}$ (K)	$L_{\rm bol}$ ($L_\odot$)	$L_{\rm sub\text{-}mm}/L_{\rm bol}$ (%)	$M_{\rm env}^{4200\ {\rm AU}}$ ($M_\odot$)
Lupus 3 MMS	$16^{\rm h}09^{\rm m}18.33^{\rm s}$	$-39°04'51.6''$	39.5	0.16	6.5	0.52

where Ω is the solid angle of the emitter, and $B(\nu, T_{\rm dust})$ is the Planck function. The dependence of τ_ν on the wavelength λ is assumed to be

$$\tau_\nu = \tau_{100}\left(\frac{\lambda}{100\ \mu{\rm m}}\right)^{-\beta}, \tag{6}$$

where τ_{100} is the optical depth at 100 μm. For this SED analysis, there are only three available data points of the *Spitzer* 70 and 160 μm, the SIMBA 1.2 mm, and the upper limits at 100 μm (we do not use the *IRAS* 60 μm data because of the poor sensitivity and spatial resolution). Therefore, it is not possible to obtain a unique solution to satisfy all the parameters with the conditions $1 < \beta < 2$ and $\tau_{100} = 1$ (Fig. 7).

From the obtained SED with the above parameter sets, we calculate the bolometric luminosity ($L_{\rm bol}$), bolometric temperature ($T_{\rm bol}$), and submillimeter-to-bolometric luminosity ratio ($L_{\rm sub\text{-}mm}/L_{\rm bol}$) delimited at 350 μm (8.57×10^{11} Hz) as

$$L_{\rm bol} = 4\pi D^2 \int_0^\infty F_\nu\, d\nu, \tag{7}$$

$$L_{\rm sub\text{-}mm}/L_{\rm bol} = \frac{\int_0^{8.57\times10^{11}} F_\nu\, d\nu}{\int_0^\infty F_\nu\, d\nu}, \tag{8}$$

$$T_{\rm bol} = 1.25 \times 10^{-11}\bar{\nu}, \tag{9}$$

where D is the distance to the source (150 pc) and $\bar{\nu}$ is the mean frequency of the graybody spectra given as (Myers & Ladd 1993; Chen et al. 1995; Froebrich et al. 2003; Rengel 2004)

$$\bar{\nu} = \frac{\int_0^\infty \nu F_\nu\, d\nu}{\int_0^\infty F_\nu\, d\nu}. \tag{10}$$

For the integrals of the above equations (eqs. [7]–[9]), we interpolate the data points with piecewise power-law functions and extrapolate to zero frequency with a ν^2 law, the same as Myers & Ladd (1993). The maximum ν is set to 1.39×10^{14} Hz, which corresponds to the shortest wavelength of detection in the K_s band. As seen in Figure 7, it is crucial to estimate fluxes around $\lambda = 100$ and 300 μm near the SED peak for the accurate estimation of $T_{\rm bol}$ and $L_{\rm bol}$. Taking only the observed values here, we obtain $T_{\rm bol} = 39.5$ K, $L_{\rm bol} = 0.16\ L_\odot$, and $L_{\rm sub\text{-}mm}/L_{\rm bol} = 0.065$ (Table 4), although further far-IR and submillimeter-wave photometries are required for more accurate estimation.

4.3.2. *Scattered Light in the Short-Wavelength Component*

As mentioned above, the Lupus 3 MMS has extended emission in the near-IR. This is most likely to be scatted light coming from the central object. This contradicts the conventional picture of Class 0 objects because they are believed to be embedded too deeply in dense gas and dust to be detected in near-IR bands. However, non–spherically symmetric envelope structure has not

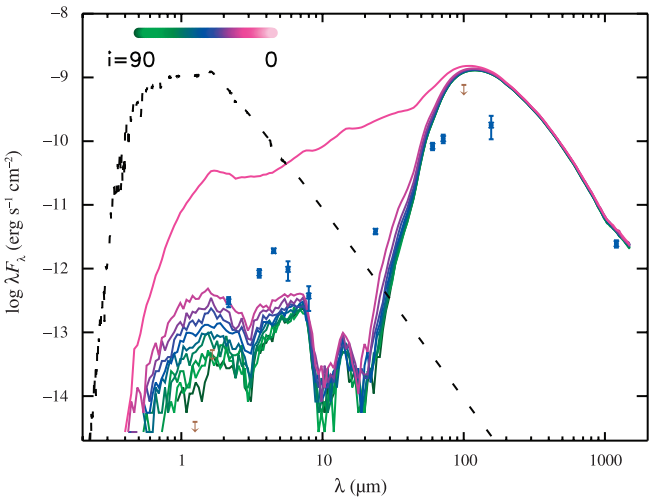

FIG. 8.—Photometric data of the Lupus 3 MMS plotted on the calculated Class 0 SED by Whitney et al. (2003b). The solid lines are the SEDs of the modeled Class 0 object seen from different viewing angles as shown by the inset color scale. The spectrum of the central object whose $T_{\rm eff}$ is 4000 K is drawn with the dashed line.

been well taken into account in Class 0 modeling. Observational studies so far have also been quite insufficient for such peculiar objects because of the small chance of having the appropriate geometries and viewing angles and because of the difficulties with infrared observations at wavelengths longward of 2 μm by ground-based telescopes.

Whitney et al. (2003a, 2003b) calculated the two-dimensional radiative transfer of young stars with circumstellar disks, envelopes, and outflow cavities and exhibited SEDs of different stellar ages with different viewing angles. In order to investigate the physical conditions of the MMS, envelope, and disk if it exists, in this subsection we compare the present data with the calculated SEDs. Figure 8 shows modeled SEDs for a Class 0 object that has a 3.73 $M_\odot$ envelope with a power-law density distribution, a constant-density cavity of 10^5 cm^{-3} whose opening angle is 5°, and a central source of 1 $L_\odot$ whose surface temperature is 4000 K (for more details, see Whitney et al. 2003b). The present data points are overplotted on their SEDs for different viewing angles. The long-wavelength component appears to match fairly well with the data points, although the model SED needs to be scaled down slightly. On the other hand, in the shorter wavelengths, the observed fluxes are significantly stronger than the modeled ones. This is probably due to the cavity opening angle used in the modeling. The K_s-band image shows that the fan-shaped low-extinction region has an angle of ~30°–45°, while the model parameters for Class 0 and late Class 0 stages are 5° and 10°, respectively. The SED of the late Class 0 case is significantly brighter in the near-IR bands, which are dominated by scattered light (see Fig. 3 of Whitney et al. 2003b). The near-IR intensity also depends on the viewing angle, and the near-IR spectral features are very complicated, with atomic and molecular lines, water ice (3.05 and 4.62 μm) and silicate absorption bands (~10 μm), and polycyclic aromatic hydrocarbon (PAH) emission (~8 μm). At the IRAC 4.5 μm band, the MMS SED shows significant enhancement compared to the model, possibly because of hydrogen recombination lines of Brα (4.05 μm) and Pfβ (4.65 μm), and molecular lines of H_2(0–0) S(9) (4.69 μm) and CO(1–0) P(8) (4.74 μm), although the H_2(1–0) S(1) line with lower excitation energy at 2.12 μm is not detected. Further spectroscopic observations and radiative transfer calculations with carefully selected physical parameters are required for consistent modeling. Here we focus only on the shortest wavelength part of the scattered light SED to investigate the properties of the central source.

Because of the nondetection in the *JH* bands, only the lower limits of the *JHK* colors can be given as $J - K_s \geq 6.4$ mag and $H - K_s \geq 2.8$ mag. These are remarkably redder than their simulated colors. It seems difficult to satisfy such a steep cutoff at the shorter end of the SED only by adjustments of the disk and envelope parameters. For these calculations, the central object as the source of the incident light is fixed with a stellar effective temperature, $T_{\rm eff}$, of 4000 K. Because light in the *JHK* bands are dominated by scattering, we scaled the fluxes at these wavelengths by adopting a lower $T_{\rm eff}$ to match the observed $J - K_s$ and $H - K_s$ colors. As a result, we obtain $T_{\rm eff} < 1400$ K for the case of Class 0 and $T_{\rm eff} < 1200$ K for late Class 0, taking into account the observed errors and the ranges of the fluxes with different viewing angles. This is far cooler than the assumed value. This modification would lead to fainter fluxes at long wavelengths by more than an order of magnitude, due to reduced radiation heating.

4.4. *Nature of the Millimeter-wave Source*

Among the samples of Froebrich (2005) the Lupus 3 MMS is one of the coldest and faintest Class 0 objects. This implies that it has a large, cold surrounding envelope, which is a unique property of young protostars. The obtained values satisfy the suggested Class 0 object criteria, which are $L_{\rm sub\text{-}mm}/L_{\rm bol} > 0.005$ and $T_{\rm bol} < 70$ K (André et al. 2000). The obtained parameters of $M_{\rm env}^{4200\ \rm AU} = 0.52\ M_\odot$, $T_{\rm bol} = 39.5$ K, and $L_{\rm bol} = 0.16\ L_\odot$ are plotted on the $L_{\rm bol}$ versus $T_{\rm bol}$ and $M_{\rm env}^{4200\ \rm AU}$ versus $L_{\rm bol}$ diagrams in Figure 9 and compared with other previously known low-mass Class 0 objects and with theoretical models (Chen et al. 1995; Myers et al. 1998; André et al. 2000; Motte & André 2001). The faint luminosity and cold temperature of the Lupus 3 MMS indicate a very young age of ~10^4 yr, which is consistent with the dynamical age derived from the molecular outflow. Because it is in a very early phase of mass accretion, the present stellar mass is negligibly small compared to the envelope mass. Hence, the expected final mass is ~0.5 $M_\odot$.

In the Lupus star-forming region, this is the second finding of a Class 0 object, the first being Barnard 228 (Shirley et al. 2000). Barnard 228 was found to have a shock-excited nebulosity (Heyer & Graham 1989) and a molecular outflow (Tachihara et al. 1996) associated with IRAS 15398−3359. The $T_{\rm bol}$ and $L_{\rm sub\text{-}mm}/L_{\rm bol}$ are estimated to be 61 K and 0.048, respectively (Chen et al. 1997; Froebrich 2005). With the relatively warm $T_{\rm bol}$, this is believed to be a borderline object between Class 0 and I and hence much more evolved than the Lupus 3 MMS.

The Lupus 3 MMS is a peculiar object in the sense that it is a Class 0 object with near-IR detections. As discussed above, it is interpreted as a young protostar embedded in a thick dust envelope with outflow cavities. Such inhomogeneous envelope configurations have been considered by several authors besides Whitney et al. (2003a, 2003b). A theoretical calculation suggests that the $T_{\rm bol}$ used as a criterion for Class 0 objects is subject to change due to geometric effects (Masunaga & Inutsuka 2000). This issue should be carefully treated in both observational and theoretical studies.

Young et al. (2004) found an object (L1014-IRS) similar to the Lupus 3 MMS with *Spitzer* in a molecular cloud (L1014) formerly believed to be a starless core. It is detected in all the *Spitzer* bands in addition to 450, 850, and 1200 μm. From the SED analysis, they calculated $T_{\rm bol} = 50$ K, $L_{\rm bol} = 0.3\ L_\odot$, and $L_{\rm sub\text{-}mm}/L_{\rm bol} = 0.05$ and concluded that it is likely to be a Class 0 object even though it does not exhibit a clear signature of molecular

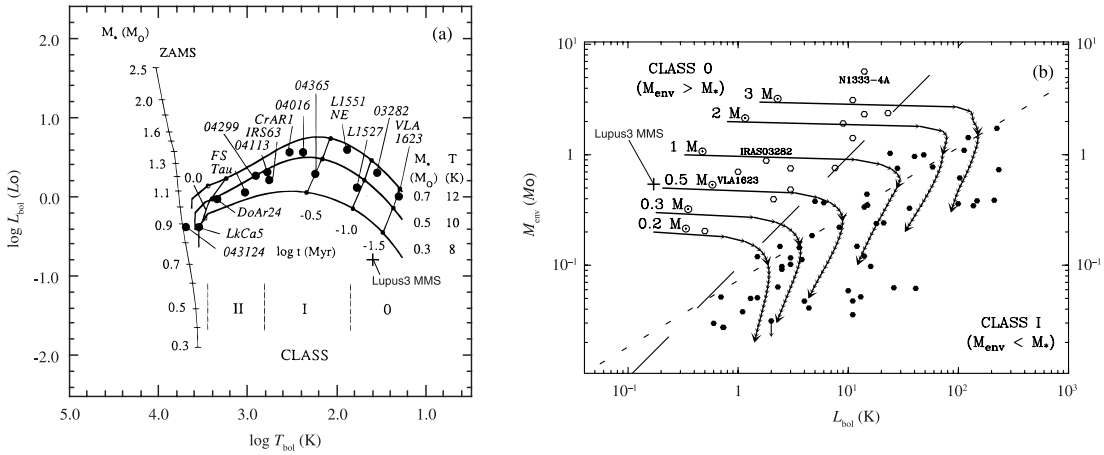

FIG. 9.—(*a*) Diagram of $L_{\rm bol}$ vs. $T_{\rm bol}$ taken from Myers et al. (1998). The three solid curves denote the evolutionary tracks of final stellar masses of 0.3, 0.5, and 0.7 $M_{\odot}$. Four times t (Myr) since the start of infall are indicated, at log $t = -1.5, -1.0, -0.5$, and 0.0. The Lupus 3 MMS is plotted as a plus sign. (*b*) Diagram of $M_{\rm env}$ vs. $L_{\rm bol}$ taken from André et al. (2000). The open and filled circles and plus sign show Class 0 and I sources and the Lupus 3 MMS, respectively. The curves denote the evolutionary tracks assuming that the accretion rate declines exponentially with time. The long-dashed and short-dashed lines are two M-$L_{\rm bol}$ relations marking the conceptual border zone between the Class 0 ($M_{\rm env} > M_*$) and the Class I ($M_{\rm env} < M_*$) stage (see André et al. 2000 for more details).

outflow. L1014-IRS is brighter in wavelengths longward of 50 μm but fainter in shorter wavelengths than the Lupus 3 MMS and has no bump between 8 and 24 μm. From the short-wavelength IRAC data, its SED gives $L = 0.025\ L_{\odot}$ and $T_{\rm eff} = 700 \pm 300$ K, also remarkably cool for surface temperature of the central object. Another detection of a known Class 0 object, IRAM 04191+1522, has been reported recently. It is believed to be an extremely young Class 0 object with very cold $T_{\rm bol}$ ($\sim$18 K) and a powerful molecular outflow (André et al. 1999) and was found by *Spitzer* to have a butterfly-like nebulosity in 4.5 μm, which correlates which the outflow configuration (Dunham et al. 2006). These very young and low luminosity objects should be treated by more sophisticated models with non–spherically symmetric conditions. Note also that none of these infrared visible Class 0 objects (including L1521F, mentioned below) have been reported to have well-collimated jets such as those seen in HH 30 and HH 34 (e.g., Ray et al. 1996), in spite of the detections of bipolar outflows and conical nebulae.

The estimates of $T_{\rm eff}$ provide a restriction on current protostellar models. According to theoretical calculations, the central temperature starts rising when the first hydrostatic core is formed (the "first core" phase) at the center of the molecular core, up until 2000 K, when molecular hydrogen is set to be dissociated (the "second collapse" phase). The lifetime of the first core is $\lesssim 10^3$ yr, and it is unlikely that such a rare phenomenon could be detected. Therefore, the lower observed $T_{\rm eff}$ than the dust sublimation temperature (1600 K) suggests that the central object is not naked but surrounded with a hot dust cocoon, unlike in Whitney's model, located at the bottom of the outflow cavity. The one-dimensional radiative transfer calculation by Masunaga & Inutsuka (2000) showed that the temperature drops down to $\sim$1000 K at $\sim$1 AU from the center, where the protostellar core should be optically thick. Hence, the outflow cavity at the bottom should be open $\gtrsim$1 AU in radius so as to expose the source of the near-IR scatted light. Alternatively, recent theoretical studies suggest that the effects of core rotation and/or magnetic fields make the first-core lifetime significantly longer and the outer surface temperature remarkably lower (Saigo & Tomisaka 2006). More accurate estimation of $T_{\rm eff}$ is achievable by spectroscopic observations to detect molecular absorption bands such as H_2O or CH_4, which will be helpful for modeling of very young protostars. With $T_{\rm eff}$ estimates for a larger number of samples, the evolutionary timescale of Class 0 objects can be assessed.

4.5. *Timescales of Dense Cores and Star Formation in Lupus*

Within the entire Lupus cloud complex, we have detected 10 $H^{13}CO^+$ cores (A. Hayashi et al. 2007, in preparation) found from 36 $C^{18}O$ cores (Hara et al. 1999). With these numbers, we discuss the timescale of the dense cores and protostars statistically. Assuming that star formation occurs constantly and straightforwardly in time, the timescale in each evolutionary stage is expected to be proportional to the number of the objects. In this region there are 196 pre–main-sequence stars (Tachihara et al. 2001), mainly found by the *Röntgensatellit* (*ROSAT*) X-ray survey, whose ages are estimated to be 7.6 Myr on average (Wichmann et al. 1997). Thus, the estimated timescale of $C^{18}O$ and $H^{13}CO^+$ cores are $\sim 1 \times 10^6$ and $\sim 4 \times 10^5$ yr, respectively, which are 3–4 times larger than the free-fall time of uniform gas spheres with densities of 10^4 and 10^5 cm^{-3}, respectively. As for Class 0 objects, on the other hand, one early-phase (the Lupus 3 MMS) and one borderline (Barnard 228) object have been found so far. Thus, the timescale of the genuine Class 0 object in Lupus is calculated to be $\sim 4 \times 10^4$ yr, which is slightly larger than but practically agrees with the conventional expectation of $\sim(1\text{–}3) \times 10^4$ yr (e.g., André et al. 2000). On the other hand, in Taurus, there are 40 $C^{18}O$ cores (Onishi et al. 1996), 55 $H^{13}CO^+$ cores (Onishi et al. 2002), two early-phase Class 0 objects, and three borderline objects. Compared to Lupus, significantly more $H^{13}CO^+$ cores are detected within clouds of comparable mass (6800 $M_{\odot}$ for Taurus and 4500 $M_{\odot}$ for Lupus in ^{13}CO), while the numbers of early-phase and borderline Class 0 objects are a few times greater.

5. SUMMARY

The Lupus 3 molecular cloud has been surveyed for dense molecular cloud cores and embedded young protostars. The major results are as follows:

1. In the Lupus 3 $C^{18}O$ core, three $H^{13}CO^+$ cores were found. Their average mass, radius, and density are 4.6 $M_{\odot}$, 0.04 pc, and 2.3×10^5 cm^{-3}, respectively. They are located a few arcminutes away from the $C^{18}O$ peak and the T associations, while they coincide with high-extinction parts whose A_V is greater than 20 mag.

2. The SIMBA observation of the dust emission at 1.2 mm detected the three dense $H^{13}CO^+$ cores, the filamentary structure along the $C^{18}O$ ridge, and a millimeter-wave point source embedded in one of the $H^{13}CO^+$ cores (core B). The masses of the dust condensations are consistent with the $H^{13}CO^+$ core masses.

3. The radial profile of the embedded MMS is represented as a slightly larger Gaussian profile than the SEST beam and smoothly connected with the outer $H^{13}CO^+$ core. It suggests that the MMS is a finite-size object with an extended envelope whose size is $\sim$7800 AU.

4. The CO($J = 3$–2) line observations by ASTE demonstrate blueshifted high-velocity wings that imply molecular outflow coming out from the MMS. It is thought to drive a molecular outflow and a jet, which has created a cavity in the core and excited the Herbig-Haro object HH 78.

5. From the 1.2 mm flux of the MMS together with the *IRAS* and *Spitzer* far-IR measurements, the MMS is very likely to be a Class 0 object with $T_{\rm bol} = 39.5$ K, $L_{\rm bol} = 0.16\ L_\odot$, $L_{\rm sub\text{-}mm}/L_{\rm bol} = 0.065$, and $M_{\rm env}^{4200\ \rm AU} = 0.52\ M_\odot$, recently formed in the $H^{13}CO^+$ core. From theoretical model calculations, this object is expected to be in the dynamical accretion phase at an age of only $\sim 10^4$ yr and have a final mass of $\sim 0.5\ M_\odot$.

6. Extended *K*-band emission is detected near the MMS, where the CO blueshifted wings and slight 1.2 mm emission excess are detected while the H_2 emission is not. These imply that the scattered light in the *K* band emerges through the outflow cavity opening by $\sim 30^\circ$–45° toward HH 78 on the near side.

7. The *Spitzer Space Telescope* archive data show that the MMS is detected in all the *Spitzer* bands. In the near-IR bands, the MMS appears as a butterfly shape, implying that the scattered light is from the bipolar cavities in contrast to the *K*-band light, which is only from the near side because of high obscuration.

8. The SED in the near-IR bands is compared with the theoretical calculations by two-dimensional radiative transfer that deals with light scattering through outflow cavities in Class 0 objects. The steep cutoff of the SED in the *JHK* band requires a relatively low temperature of the central object of $T_{\rm eff} \leq 1400$ K.

We are grateful to all the staff of the European Southern Observatory for their great hospitality. This publication makes use of the SIMBAD database by CDS, Strasbourg, France. We also thank Paula Teixeira and Kazuhito Dobashi for providing their extinction maps, Markus Mugrauer for helping with the infrared data reduction, and Atsushi Hara for helping with the observations. The MOPSIC software was developed and provided to observers by Robert Zylka. K. T. is financially supported by the Japanese Society for the Promotion of Science (JSPS). M. R. wishes to acknowledge financial support from the Deutsche Forchungsgemeinschaft (DFG) through grant Ei 409 6-2 during part of this work. This work was supported by The 21st Century COE Program: Origin and Evolution of Planetary Systems of MEXT of Japan.

REFERENCES

André, P., Motte, F., & Bacmann, A. 1999, ApJ, 513, L57
André, P., Ward-Thompson, D., & Barsony, M. 1993, ApJ, 406, 122
———. 2000, in Protostars and Planets IV, ed. V. Mannings, A. P. Boss, & S. S. Russell (Tucson: Univ. Arizona Press), 59
Bourke, T. L., et al. 2006, ApJ, 649, L37
Cambrésy, L. 1999, A&A, 345, 965
Chen, H., Grenfell, T. G., Myers, P. C., & Hughes, J. D. 1997, ApJ, 478, 295
Chen, H., Myers, P. C., Ladd, E. F., & Wood, D. O. S. 1995, ApJ, 445, 377
Chini, R., et al. 2003, A&A, 409, 235
Cohen, M., & Kuhi, L. V. 1979, ApJS, 41, 743
Comeron, F., Rieke, G. H., Burrows, A., & Rieke, M. J. 1993, ApJ, 416, 185
Crapsi, A., Caselli, P., Walmsley, C. M., Tafalla, M., Lee, C. W., Bourke, T. L., & Myers, P. C. 2004, A&A, 420, 957
Dunham, M. M., et al. 2006, ApJ, 651, 945
Evans, N. J., II, et al. 2003, PASP, 115, 965
Froebrich, D. 2005, ApJS, 156, 169
Froebrich, D., Smith, M. D., Hodapp, K.-W., & Eislöffel, J. 2003, MNRAS, 346, 163
Hara, A., Tachihara, K., Mizuno, A., Onishi, T., Kawamura, A., Obayashi, A., & Fukui, Y. 1999, PASJ, 51, 895
Herbig, G. H., & Bell, K. R. 1988, Third Catalog of Emission Line Stars of the Orion Population (Santa Cruz: Lick Obs.)
Heyer, M. H., & Graham, J. A. 1989, PASP, 101, 816
Hughes, J., Hartigan, P., Krautter, J., & Kelemen, J. 1994, AJ, 108, 1071
Kirk, J. M., Ward-Thompson, D., & André, P. 2005, MNRAS, 360, 1506
Lee, J.-E., Evans, N. J., II, Shirley, Y. L., & Tatematsu, K. 2003, ApJ, 583, 789
Masunaga, H., & Inutsuka, S. 2000, ApJ, 531, 350
Motte, F., & André, P. 2001, A&A, 365, 440
Motte, F., André, P., & Neri, R. 1998, A&A, 336, 150
Myers, P. C., Adams, F. C., Chen, H., & Schaff, E. 1998, ApJ, 492, 703
Myers, P. C., & Ladd, E. F. 1993, ApJ, 413, L47
Nakajima, Y., et al. 2003, AJ, 125, 1407
Oasa, Y., Tamura, M., & Sugitani, K. 1999, ApJ, 526, 336
Onishi, T., Mizuno, A., & Fukui, Y. 1999, PASJ, 51, 257
Onishi, T., Mizuno, A., Kawamura, A., Ogawa, H., & Fukui, Y. 1996, ApJ, 465, 815
Onishi, T., Mizuno, A., Kawamura, A., Tachihara, K., & Fukui, Y. 2002, ApJ, 575, 950
Ray, T. P., Mundt, R., Dyson, J. E., Falle, S. A. E. G., & Raga, A. C. 1996, ApJ, 468, L103
Rengel, M. 2004, Ph.D. thesis, Friedrich-Schiller-Univ. Jena
Saigo, K., & Tomisaka, K. 2006, ApJ, 645, 381
Schwartz, R. D. 1977, ApJS, 35, 161
Shirley, Y. L., Evans, N. J., II, Rawlings, J. M. C., & Gregersen, E. M. 2000, ApJS, 131, 249
Tachihara, K., Dobashi, K., Mizuno, A., Ogawa, H., & Fukui, Y. 1996, PASJ, 48, 489
Tachihara, K., Onishi, T., Mizuno, A., & Fukui, Y. 2002, A&A, 385, 909
Tachihara, K., Toyoda, S., Onishi, T., Mizuno, A., Fukui, Y., & Neuhäuser, R. 2001, PASJ, 53, 1081
Teixeira, P. S., Lada, C. J., & Alves, J. F. 2005, ApJ, 629, 276
Terebey, S., Fich, M., Noriega-Crespo, A., Padgett, D. L., Sullivan, A., & Taurus *Spitzer* Data Team. 2005, poster at Protostars and Planets V (Waikoloa Village)
Wang, Y., Jaffe, D. T., Graf, U. U., & Evans, N. J., II. 1994, ApJS, 95, 503
Whitney, B. A., Wood, K., Bjorkman, J. E., & Cohen, M. 2003a, ApJ, 598, 1079
Whitney, B. A., Wood, K., Bjorkman, J. E., & Wolff, M. J. 2003b, ApJ, 591, 1049
Wichmann, R., Krautter, J., Covino, E., Alcala, J. M., Neuhaeuser, R., & Schmitt, J. H. M. M. 1997, A&A, 320, 185
Young, C. H., et al. 2004, ApJS, 154, 396